

1 **A Fast Monotone Discretization of the Rotating**
2 **Shallow Water Equations**

3 **Guillaume Roulet¹, Tugdual Gaillard¹**

4 ¹Univ. Brest, CNRS, IRD, Ifremer, Laboratoire d'Océanographie Physique et Spatiale (LOPS), IUEM,
5 Brest, France

6 **Key Points:**

- 7 • Use WENO reconstructions on the mass flux and on the nonlinear Coriolis term
8 • Reach low level of energy dissipation and high accuracy on material conservation
9 of potential vorticity
10 • Express the continuous equations with index coordinates, finite volume quanti-
11 ties, covariant and contravariant components of the velocity
12 • Minimize the number of operations and maximize the arithmetic intensity
13 • Achieve 2 GFlop per second per core with a pure Python code

Corresponding author: Guillaume Roulet, roulet@univ-brest.fr

14 **Abstract**

15 This paper presents a new discretization of the rotating shallow water equations and a
 16 set of decisions, ranging from a simplification of the continuous equations down to the
 17 implementation level, yielding a code that is fast and accurate. Accuracy is reached by
 18 using WENO reconstructions on the mass flux and on the nonlinear Coriolis term. The
 19 results show that the build-in mixing and dissipation, provided by the discretization, al-
 20 low a very good material conservation of potential vorticity and a minimal energy dis-
 21 sipation. Numerical experiments are presented to assess the accuracy, which include a
 22 resolution convergence, a sensitivity on the the free-slip vs. no-slip boundary conditions,
 23 a study on the separation of waves from vortical motions. Speed is achieved by a series
 24 of choices rather than a single recipe. The main choice is to discretize the covariant form
 25 written in index coordinates. This form, rooted in the discrete differential geometry, re-
 26 moves most of the grid scale terms from the equations, and keep them only where they
 27 should be. The model objects appearing in resulting continuous equations have a nat-
 28 ural correspondence with the grid cell features. The other choices are guided by the max-
 29 imization of the arithmetic intensity. Finally this paper also proves that a pure Python
 30 implementation is not only possible but also very fast, thanks to the possibility of hav-
 31 ing compiled Python. As a result, the code performs 2 TFlop per second using thousand
 32 cores.

33 **Plain Language Summary**

34 Using a simplified model of the ocean and atmosphere dynamics, this paper presents
 35 a set of numerical and programming decisions that yields a code that is both fast and
 36 accurate. The accuracy is assessed in terms of capacity of the code to maintain dynamic
 37 structures over long periods of time while avoiding the emergence of numerical noise in
 38 the solution. Accuracy is achieved by using a very accurate discretization on two deci-
 39 sive terms of the model equations. Speed is achieved by a series of choices ranging from
 40 a simplification of the continuous equations down to the implementation level. This pa-
 41 per also proves that a pure Python code is a viable alternative to perform simulations
 42 on high performance computing centers with as much as 2 TFlop per second using thou-
 43 sand cores.

1 Introduction

The rotating shallow water (RSW) equations are the perfect framework to test concepts, methods and ideas for later applications to more sophisticated atmospheric or oceanic models. When it comes to numerical modeling, two goals are particularly important: speed and accuracy. They are rather antagonistic for accuracy comes with higher order schemes, which are computationally more expensive than low order ones, therefore penalizing speed. However things are more subtle because a higher order discretization in time may allow a larger time step, whereas a higher order discretization in space may increase the effective resolution, allowing to use a coarser grid. The price of having high-order discretizations may thus be largely compensated. In this paper we show how the WENO reconstruction (Jiang & Shu, 1996), a highly computationally demanding scheme, can be used in a RSW model on both the continuity and the momentum equations to provide high accuracy, while still allowing a very fast code. The merits are such that this numerical method opens the way for a new class of sub-grid-scale closure.

Having a code running fast is a very valuable quality. For a given amount of computational resources, it allows for a longer time integration or a greater spatial resolution. Achieving speed involves many design choices, rather than one, that include the programming language, the algorithms implementation and the code design in general. When measured in terms of floating point operations (Flop) per second, the speed issue rapidly touches to the hardware architecture. The question should be, for a given computer, how close is the code speed to the maximum speed achievable on this computer. The maximum speed is given by the clock frequency but, if the code involves too much data transfer between the memory and the CPU, the effective speed can be far from this maximum. Indeed, according to the roof-line model (Williams et al., 2009), the speed might be memory-bound or compute-bound, and that depends on the arithmetic intensity, which is the ratio of the number of Flop per float exchanged between the memory and the core. To achieve the optimal speed, a code should be in the compute-bound region, namely it should have a large enough arithmetic intensity, which means to perform as many Flop on the data, once the data have been transferred to the core. This issue is often overlooked in atmosphere and ocean models.

Increasing the arithmetic intensity is not so easy. We are aware of at least three techniques. First, this can be done by blending many operations into a few large loops,

76 as opposed to having many loops each doing one operation. A typical example of code
 77 following this approach is ROMS (Shchepetkin & McWilliams, 2005). This technique comes
 78 at the expend of code readability and modularity, which makes code evolutions harder,
 79 e.g. changing the time stepping. The second possibility is to use numerical discretiza-
 80 tions that require more Flop per grid point. A very good example of such demanding
 81 computation is a high order WENO reconstruction (Shu, 1999), which loops back on
 82 the question of accuracy. Indeed, replacing linear schemes with high-order non-linear schemes
 83 not only increases the arithmetic intensity, but it also increases the model accuracy. This
 84 is the main point of this paper. We elaborate on the benefits of WENO reconstruction
 85 below.

86 The third technique is to simply reduce the number of Flop, and the associated data
 87 transfer. This might sound odd but there is actually an obvious way, though neglected:
 88 strip down the RSW equations to a minimal covariant form. The discretized RSW equa-
 89 tions, when written either in curvilinear coordinates or on non rectangular grids, are usu-
 90 ally cluttered with a lot of grid scale factors multiplications (lengths, inverse of lengths
 91 and areas). In this paper we show how these scale factors can be removed almost every-
 92 where in the vector invariant form of the RSW equations. The price is to slightly change
 93 the objects the code manipulates. Without further explanations yet, the changes are the
 94 following: use the array indices (i, j) as spatial coordinates, use finite volume quantities
 95 carrying their area, replace the velocity components with the pairs of covariant and con-
 96 travariant components. These changes arise naturally from the discrete differential ge-
 97 ometry (Desbrun et al., 2006; Cotter & Thuburn, 2014), which identifies the basic ob-
 98 jects such as scalars, vectors, vorticity, as differential forms and which connects them with
 99 the grid features, respectively cells, edges and vertices, while emphasizing the crucial dif-
 100 ference between the primal and the dual mesh. To avoid burying the ideas into an over-
 101 whelming formalism, we will start from known grounds and make the concepts emerge
 102 naturally. For the reader tempted to know more we may suggest this very tutorial pa-
 103 per (Perot & Zusi, 2014). The obtained simplified form of the RSW equations has many
 104 advantages. It is light, in terms of operations involved ; it is fully adapted to a discretiza-
 105 tion on a logically rectangular C-grid ; and, last but not least, it is covariant, in the sense
 106 that the form is invariant under a change of coordinates. Thanks to the covariance the
 107 space is really seen as an array of cells, even on the continuous equations.

108 As already mentioned, the programming language is central. Until recently the climate-
 109 atmospheric-ocean community mostly relied on Fortran and MPI. Fortran has long been
 110 considered as the ultimate language for HPC. Things are changing. New codes in Cython
 111 or Julia (Ramadhan et al., 2020) are now popping up quite regularly. But pure Python
 112 codes remain rare, mostly because Python is an interpreted language. This can now be
 113 overcome thanks to the numba module (Lam et al., 2015) that allows to compile Python.
 114 This paper proves that all the ideas presented so far can be implemented in a pure Python
 115 code, while reaching 2.0 GFlop per second on a 2.5 GHz core, and 2.0 TFlop per sec-
 116 ond on the same architecture with a thousand cores.

117 Finally another possibility to increase the speed is to trade it with accuracy by us-
 118 ing single precision floats, or even a blend of a single precision and BFloats (two bytes
 119 floats), which de facto reduces the memory traffic and the time of each Flop. This ap-
 120 proach has been recently tested quite thoroughly (Klöwer et al., 2020).

121 Let us now turn on the accuracy aspect. Accuracy encompasses several properties.
 122 In this paper we are particularly interested in the ability: i) to have minimal energy dis-
 123 sipation, ii) to materially conserve the potential vorticity (PV), iii) to maintain noise-
 124 free PV, iv) to separate vortical motions from wave motions and v) to enforce clean lat-
 125 eral boundary conditions, either free or no-slip. We achieve these properties with essen-
 126 tially one key idea: use WENO reconstructions on the mass flux and the nonlinear Cori-
 127 olis term, namely the two decisive terms that control these properties.

128 Using a WENO reconstruction on the nonlinear Coriolis term may seem odd be-
 129 cause the upwinding breaks the invariance under the time reversal symmetry, which un-
 130 avoidably introduces dissipation. The opposite strategy for accuracy is to seek a sym-
 131 plectic integrator (Brecht et al., 2019). There are in fact several good reasons for using
 132 WENO. First, a close inspection of the RSW equations written in vector-invariant form
 133 reveals the equal importance in the material conservation of PV of the mass flux and the
 134 nonlinear Coriolis term, which is a vorticity flux. So if one applies a WENO reconstruc-
 135 tion on the mass flux, to provide mixing, it is appealing to proceed similarly on the non-
 136 linear Coriolis term to have a consistent discretization of the PV and to ensure maxi-
 137 mum symmetry between the two fluxes. We will show that this technique brings the afore-
 138 mentioned properties on the PV dynamics. Second, from the energy point of view, the
 139 nonlinear Coriolis term should have a vanishing work, but if we consider the filtered ver-

140 sion of the RSW equations in vector-invariant form, following the LES filter technique
 141 (Sagaut, 2006), then, once again, the nonlinear Coriolis term turns out to be the key player.
 142 Indeed, the vector-invariant form transforms the momentum flux into the nonlinear Cori-
 143 olis term and the gradient of kinetic energy term. These two terms play a very differ-
 144 ent role on the energy equation. The gradient term becomes the divergence of the ki-
 145 netic energy flux whereas the nonlinear Coriolis term turns out to be the term respon-
 146 sible for the exchange of energy between the resolved grid scales and the sub-grid scales.
 147 Therefore advocating for using the WENO reconstruction to compute this term. The
 148 third, and last reason was originally formulated by Mullen et al. (2011). If we let the dif-
 149 ferential geometry guides our numerical choices, then the transport of the momentum
 150 should be discretized in such way that it obeys the properties of the Lie derivative. This
 151 pleads for upwinding the vorticity in the nonlinear Coriolis term. If one also demands
 152 high order discretization and monotonicity, then a WENO reconstruction is a natural
 153 solution. Note that WENO reconstructions have already been tested for shallow water
 154 models (Xing & Shu, 2005; Noelle et al., 2007; Gallerano & Cannata, 2011) but it was
 155 on the flux form of the momentum equation. Applying it on the nonlinear Coriolis term
 156 is completely new to our knowledge.

157 From the more general perspective of large eddy simulations (LES) models, the idea
 158 stems from the MILES approach (Boris et al., 1992). MILES was designed for three di-
 159 mensional models as an alternative to physically based explicit closures, typically the Smagorin-
 160 sky closure or one of its variant. In ILES the closure takes the form of a monotonic dis-
 161 cretization of the mass and momentum fluxes. Such closure is coined *implicit* (Margolin
 162 et al., 2006) or *numerical* (Pope, 2004). A numerical closure is opposed to a physical or
 163 purely physical closure for which there is a physical model supporting the closure. The
 164 use a monotonic discretization on the nonlinear Coriolis term rather than on the momen-
 165 tum flux, can be seen as a variant of the MILES approach. This paper adds up to the
 166 list of closures for LES models solving the RSW equations (Graham & Ringler, 2013).

167 This paper is organized as follows. In Section 2, we show how the continuous RSW
 168 equations can be strip down to a very simple form while still handling general curvilinear
 169 coordinates and being fully covariant. We discuss the material conservation of PV
 170 to motivate the discretization, which is presented in Section 3. In Section 4, implemen-
 171 tation choices are described and the code speed is assessed. In Section 5, the accuracy

172 of the code is tested with three experiments, each assessing one aspect. A summary is
 173 given in Section 6.

174 **2 A fresh look at the RSW equations**

175 The goal of this section is to present the RSW equations in the form that it is well
 176 suited for having a fast and accurate numerical model, namely

$$177 \quad \frac{\partial \mathbf{u}}{\partial t} = -(\zeta^* + f^*) \mathbf{U}^\perp - \nabla (g(h + b) + k) \quad (1)$$

$$178 \quad \frac{\partial h^*}{\partial t} = -\nabla \cdot (h^* \mathbf{U}) \quad (2)$$

$$179 \quad \zeta^* = \nabla \times \mathbf{u} \quad (3)$$

$$180 \quad k = \frac{1}{2} \mathbf{u} \cdot \mathbf{U} \quad (4)$$

181 which is the vector invariant form slightly in disguise. Indeed, at this stage only four terms
 182 have their classical definition: h , the layer depth, g is the acceleration due to gravity, b
 183 the bottom topography and k the kinetic energy density. The other terms require more
 184 context before being fully defined. In particular the meaning of the \star decorator and the
 185 use of two different terms \mathbf{u} and \mathbf{U} for the velocity will be explained. The $^\perp$ symbol on
 186 \mathbf{U}^\perp has its usual meaning, it designates the quarter turn counterclockwise rotated \mathbf{U} .

187 **2.1 Index coordinates**

188 We start by endowing the space with a mapping system. The most general way is
 189 to use curvilinear coordinates (η_1, η_2) . They might be Cartesian (x, y) , spherical (ϕ, θ) ,
 190 cylindrical (r, θ) , or any other. Among the other possibilities are the index coordinates
 191 (i, j) , associated with a logically rectangular grid. These coordinates, which are grid res-
 192 olution dependent, are natural to locate grid cell features such as centers, edges, and ver-
 193 tices because all the variables are mapped with only integers or half integers indices, de-
 194 pending on the variable staggering. But their most interesting property is that two ad-
 195 jacent points of the same feature in the direction either i or j are separated by either
 196 $di = 1$ or $dj = 1$. Thus, the partial derivative $\partial\phi/\partial i$ of a field $\phi(i, j)$ is naturally dis-
 197 cretized as

$$198 \quad \frac{\partial\phi}{\partial i} \rightarrow \phi[i + 1, j] - \phi[i, j], \quad (5)$$

199 with no division, because $di = 1$. By using index coordinates, a spatial derivative boils
 200 down to one subtraction. This is the first optimization and simplification of this paper.

201 For the rest of this paper, we will use the index coordinates, therefore using (i, j) instead
 202 of (η_1, η_2) . The consequence is that the ∇ operator reads

$$203 \quad \nabla = \left(\frac{\partial}{\partial i}, \frac{\partial}{\partial j} \right), \quad (6)$$

204 and its discretized version only involves the two points differences (5).

205 Once the coordinates system is defined, the space must be equipped with a met-
 206 ric to measure the distance between two nearby points, say P_1 at (i, j) and P_2 at $(i+$
 207 $di, j + dj)$. This is achieved with the first fundamental form

$$208 \quad ds^2 = e_1^2 di^2 + e_2^2 dj^2 \quad (7)$$

209 where $e_1(i, j)$ and $e_2(i, j)$ describe the metric of the space. For the index coordinates sys-
 210 tem, (e_1, e_2) are the elementary distances between two points separated either by $(1, 0)$
 211 in the direction i , or by $(0, 1)$ in the direction j . In other words, (e_1, e_2) are the grid cell
 212 lengths and they carry the length dimension. For other coordinates systems, e_1 and e_2
 213 may not have the dimensions of a length, e.g. in the Cartesian coordinate case $(e_1, e_2) =$
 214 $(1, 1)$, or not have the same dimension, e.g. in the cylindrical coordinate case $(e_1, e_2) =$
 215 $(1, r)$.

216 **2.2 Finite volumes and contravariant components**

217 To present the second optimization and simplification, let us recall how the equa-
 218 tions in curvilinear coordinates are usually written. In particular, the continuity equa-
 219 tion $\partial h / \partial t = -\nabla \cdot (h \tilde{\mathbf{u}})$, where $\tilde{\mathbf{u}} = (\tilde{u}, \tilde{v})$ is the velocity, reads

$$220 \quad \frac{\partial h}{\partial t} = -\frac{1}{e_1 e_2} \left(\frac{\partial}{\partial i} (h \tilde{u} e_2) + \frac{\partial}{\partial j} (h \tilde{v} e_1) \right). \quad (8)$$

221 This equation, though absolutely correct, is unnecessarily cluttered. The drawbacks are
 222 many. Beyond the code readability, it harms the code speed because it requires unnec-
 223 essary multiplications and unnecessary data transfer from the memory to the CPU, as
 224 e_1 and e_2 are also bi-dimensional arrays in the general case. It also makes the interpo-
 225 lation of model variables more involved. (8) can be simplified into (2), viz.

$$226 \quad \frac{\partial h^*}{\partial t} = -\frac{\partial}{\partial i} (h^* U) - \frac{\partial}{\partial j} (h^* V) \quad (9)$$

227 with no sacrifice, by simply defining

$$228 \quad h^* = h e_1 e_2, \quad \text{and} \quad \mathbf{U} = (U, V) = (\tilde{u}/e_1, \tilde{v}/e_2). \quad (10)$$

229 (9) now involves only two multiplications, that correspond to a genuine non-linearity of
 230 the RSW equations, and three additions/subtractions. The grid scale factors are gone.
 231 The price to pay is to accept working with the less intuitive variables (h^*, \mathbf{U}) rather than
 232 the usual “physical” $(h, \tilde{\mathbf{u}})$. The benefits are considerable: computationally, implemen-
 233 tation wise and even conceptually. The simplification neither comes by chance or is a
 234 mathematical trick. (9) exposes the geometric nature of the objects we should manip-
 235 ulate. Let us comment on these two variables.

236 The first realization is that the velocity which fluxes the mass is \mathbf{U} , whose dimen-
 237 sions are T^{-1} . \mathbf{U} turns out to be the contravariant form of the velocity in the index co-
 238 ordinates system. The second realization is the use of h^* . As the product of h with the
 239 area $A = e_1 e_2$, h^* is naturally the *amount* of h , i.e. the finite volume version of h . The
 240 discretized version of h^* should be natural for every numerical modeler but its contin-
 241 uous version might be a bit more mysterious. It is worth an explanation. In the contin-
 242 uous equations, A is an infinitesimal surface area. In Cartesian coordinates, A would be
 243 $dx dy$ and h^* would be $h dx dy$. This might look awkward, but it is not, for there is a solid
 244 underlying mathematical theory: the differential geometry. In this paper we have decided
 245 to not use the artillery of differential geometry because it would overwhelm the discus-
 246 sion with too many concepts. However, it is with these concepts in mind that this work
 247 has been carried out. The reader interested in the connection with the differential ge-
 248 ometry may look at these papers. The present paper is really aimed at numerical mod-
 249 elers. A consequence of h^* carrying its infinitesimal area is that it can be used as is in
 250 a domain integration. For instance, the total volume is $V = \int h^*$.

251 **2.3 Covariant components**

252 Similarly the momentum equations in curvilinear coordinates vector-invariant form
 253 usually read

$$254 \quad \frac{\partial \tilde{u}}{\partial t} = (\zeta + f)\tilde{v} - \frac{1}{e_1} \frac{\partial}{\partial i} \left(g(h + b) + \frac{1}{2} |\tilde{\mathbf{u}}|^2 \right) \quad (11)$$

$$255 \quad \frac{\partial \tilde{v}}{\partial t} = -(\zeta + f)\tilde{u} - \frac{1}{e_2} \frac{\partial}{\partial j} \left(g(h + b) + \frac{1}{2} |\tilde{\mathbf{u}}|^2 \right), \quad (12)$$

256 where f is the Coriolis parameter and ζ is the vorticity

$$257 \quad \zeta = \frac{1}{e_1 e_2} \left(\frac{\partial}{\partial i} (e_2 v) - \frac{\partial}{\partial j} (e_1 u) \right). \quad (13)$$

258 (12) can be transformed into (1), viz.

$$259 \quad \frac{\partial u}{\partial t} = (\zeta^* + f^*)V - \frac{\partial}{\partial i} (g(h + b) + k) \quad (14)$$

$$260 \quad \frac{\partial v}{\partial t} = -(\zeta^* + f^*)U - \frac{\partial}{\partial j} (g(h + b) + k) \quad (15)$$

by defining

$$\mathbf{u} = (u, v) = (\tilde{u} e_1, \tilde{v} e_2), \quad (16)$$

261 and

$$262 \quad f^* = f e_1 e_2, \quad \zeta^* = \frac{\partial v}{\partial i} - \frac{\partial u}{\partial j} \quad \text{and} \quad k = \frac{1}{2} \mathbf{u} \cdot \mathbf{U}. \quad (17)$$

263 As in the continuity equation, no grid lengths are involved in either the gradient or the
 264 curl. The vector \mathbf{u} has two interpretations: it is both a circulation element, and the co-
 265 variant form of the velocity in the index coordinates system. By combining the defini-
 266 tions of \mathbf{u} and \mathbf{U} we have $(u, v) = (U e_1^2, V e_2^2)$. This relation can be written in tensor
 267 notation $\mathbf{u} = \mathbf{g} \mathbf{U}$, with

$$268 \quad \mathbf{g} = \begin{pmatrix} e_1^2 & 0 \\ 0 & e_2^2 \end{pmatrix} \quad (18)$$

269 the metric tensor. The dimensions of the covariant components are $L^2 T^{-1}$. Therefore
 270 neither \mathbf{u} or \mathbf{U} have the dimensions LT^{-1} of a speed. The distinction between \mathbf{u} and
 271 \mathbf{U} may seem quite artificial and formal at first. It turns out that they correspond to two
 272 very different substances: \mathbf{u} is the momentum, the dynamical quantity that is transported
 273 and that obeys a conservation law, whereas \mathbf{U} is the flux, the kinematic quantity that
 274 transports things. ζ^* has the same dimensions as \mathbf{u} and satisfies $\zeta^* = \zeta e_1 e_2$. Conse-
 275 quently ζ^* can be seen either as an elementary circulation along a closed loop, or as the
 276 usual vorticity times the area element, i.e. the finite volume version of ζ . Likewise, f^*
 277 is the finite volume version of the planetary vorticity f . At this stage, (9-10, 14-17) are
 278 in the form we use for the discretization.

279 **2.4 Potential vorticity**

280 A central diagnostic quantity of the RSW equations is $q = (\zeta^* + f^*)/h^*$, the po-
 281 tential vorticity, abbreviated PV throughout this paper. PV plays a central role in ro-
 282 tating flows for it allows to split the dynamics into a balanced part, captured by the PV
 283 evolution, and the unbalanced, the gravity waves, that propagate with vanishing net PV
 284 transport. Being a ratio of two finite volume quantities, q is a density, as opposed to a

285 finite volume quantity. It obeys $\partial q/\partial t + \mathbf{U} \cdot \nabla q = 0$, which expresses the material con-
 286 servation on fluid parcels. This conservation law is highly desirable at the numerical level.
 287 It should be emphasized that the material conservation is much more demanding numer-
 288 ically than a global conservation. In practice, it means that the probability density func-
 289 tion of q remains stationary in time. Ensuring exact material conservation of this derived
 290 quantity is possible on steady flows, e.g. the cases 2 and 3 of (Williamson et al., 1992),
 291 but it is impossible on arbitrary flows, for a fundamental reason. Indeed, the material
 292 conservation holds as long as there is no dissipation nor mixing, viz. for inviscid flows
 293 but, sooner or later, mixing of PV kicks in. This is because of the tendency for the PV
 294 to develop filaments that, under the flow deformation, elongate and get thinner with time,
 295 a process known as the direct cascade of enstrophy. For RSW equations the enstrophy
 296 density is $q^2 h$ and for inviscid flows, the total enstrophy, integrated over the domain,
 297 $Z = \int q^2 h^*$ should be conserved. In a numerical model the direct cascade of enstro-
 298 phy should proceed as inviscidly as possible across the resolved scales until it reaches the
 299 grid scale, at which point the numeric should be helped to parameterize the unresolved
 300 cascade continuation. This parameterization usually boils down to dissipate the enstro-
 301 phy at the grid scale. In this paper we adopt the MILES approach consisting in using
 302 monotonic upwinded reconstructions to provide the required dissipation of enstrophy.
 303 But the tricky point is that q is essentially a by-product of the equations, there is no di-
 304 rect handle on the PV evolution. The PV dynamics is controlled only through the dy-
 305 namics of h^* and $\omega^* = \zeta^* + f^*$, the finite volume absolute vorticity. To complicate even
 306 more, ω^* is also a derived quantity, but fortunately, the vector invariant form exposes
 307 the ω^* dynamics in plain sight offering a way to consistently handle h^* and ω^* .

308 The numerical discretization we propose aims at having a PV material conserva-
 309 tion as good as possible. The material conservation is not a mere coincidence, it corre-
 310 sponds to a hidden symmetry of the equations: the invariance of the equations under a
 311 relabeling of the parcels. Enforcing material conservation discretely is thus a way to sat-
 312 isfy this hidden symmetry of the equations. For that we adopt a slight change of per-
 313 spective on the role of q in the numerical integration. Instead of focusing on q , we fo-
 314 cus on ω^* . Indeed, in practice, the material conservation of PV derives from a subtle can-
 315 cellation in the momentum and the continuity equation between the vorticity flux $\omega^* \mathbf{U}$
 316 and the mass flux $h^* \mathbf{U}$. Let us carefully examine how this cancellation works for this will
 317 suggest a new way to discretize the RSW equations.

318 To derive the material conservation of PV we apply the chain rule on

$$319 \quad \frac{\partial q}{\partial t} = \frac{1}{h^{*2}} \left(h^* \frac{\partial \omega^*}{\partial t} - \omega^* \frac{\partial h^*}{\partial t} \right) \quad (19)$$

320 that reveals the very symmetrical role between the continuity equation and the the equa-
 321 tion for the absolute vorticity. The latter is derived by taking the curl of (1), namely

$$322 \quad \frac{\partial \omega^*}{\partial t} = -\nabla \cdot (\omega^* \mathbf{U}), \quad (20)$$

323 which expresses that the vorticity obeys a conservation law in flux form, exactly like h^* .

324 Substituting (20) in (19) yields

$$325 \quad \frac{\partial q}{\partial t} = \frac{1}{h^{*2}} (-h^* \nabla \cdot (\omega^* \mathbf{U}) + \omega^* \nabla \cdot (h^* \mathbf{U})) \quad (21)$$

$$326 \quad = -\frac{1}{h^{*2}} \left[h^* \mathbf{U} \cdot \nabla \omega^* - \omega^* \mathbf{U} \cdot \nabla h^* + \underbrace{h^* \omega^* \nabla \cdot \mathbf{U} - h^* \omega^* \nabla \cdot \mathbf{U}}_{=0} \right] \quad (22)$$

$$327 \quad = -\mathbf{U} \cdot \nabla q. \quad (23)$$

328 We see that the material conservation arises because of the cancellation of the two terms
 329 in (22), which follows from the identity

$$330 \quad \nabla \cdot (\phi^* \mathbf{U}) = \mathbf{U} \cdot \nabla \phi^* + \phi^* \nabla \cdot \mathbf{U}, \quad (24)$$

331 where ϕ^* is either h^* or ω^* . On a C-grid, the discrete version of this identity can be made
 332 exact provided the quantity ϕ^* , in the flux $\phi^* \mathbf{U}$, is interpolated at velocity point.

333 The discretization we propose is now clear: use monotonic high-order biased re-
 334 construction of ω^* and h^* to estimate the terms $\omega^* \mathbf{U}^\perp$, in the momentum equation, and
 335 $h^* \mathbf{U}$, in the continuity equation. For the mass flux, this is the usual upwind interpola-
 336 tion. For the nonlinear Coriolis term the upwinding should be done in the direction of
 337 the flux, namely \mathbf{U}^\perp , not in the direction of the momentum on which it applies. This
 338 is the main originality of this paper.

339 3 Discretization

340 We now present the model discretization by going through three aspects: the space
 341 and time discretizations ; and the handling of the boundary conditions.

342 3.1 Space discretization

343 The model equations are discretized on a logically rectangular C-grid. In the C-
 344 grid there is a natural distinction between the *primal* grid and the *dual* grid (Figure 1a).

345 In this paper we chose to map the primal grid centers with integer indices and the dual
 346 grid centers with half integer indices. The velocity components, both covariant and con-
 347 travariant, are defined on the edges of the dual grid, h^* is defined at cell centers of the
 348 primal grid and the vorticity terms ζ^* and f^* are defined at cell centers of the dual grid,
 349 which are also the vertices of the primal grid. The rotated \mathbf{U}^\perp is defined on the edges
 350 of the primal grid, which implies that its components are staggered compared to the com-
 351 ponents of \mathbf{U} (Figure 1a). Following the C-grid terminology, we denote “u-point” and
 352 “v-point” the place where u and v are discretized.

353 Because we use the index coordinates (i, j) , the model equations are completely obliv-
 354 ious to e_1 and e_2 , the grid scale factors, which means that for u , v and h^* the space is
 355 seen as an array of regular indices, regardless of the underlying metric. Consequently the
 356 grid cells are truly squares, of size 1×1 in the index units. This also means that spa-
 357 tial interpolations, involved in the evaluation at non native locations, should be done on
 358 the regular grid of indices, not on the irregular grid of spatial locations.

359 Before giving the discretized equations we define three spatial operators. The first
 360 one is the finite difference operator

$$361 \quad \delta_{i+1/2}[\phi] = \phi_{i+1} - \phi_i \quad (25)$$

362 estimating the along i partial derivative of ϕ at location $i+1/2$ assuming ϕ is discretized
 363 at integer locations along i . The converse is also needed $\delta_i[\phi] = \phi_{i+1/2} - \phi_{i-1/2}$ to es-
 364 timate a partial derivative at location i using a quantity discretized at half integer lo-
 365 cations. To designate an along j partial derivative we should use either $\delta_j[\phi]$ or $\delta_{j+1/2}[\phi]$.

366 The two others are interpolation operators, interpolating along direction i (or along
 367 the j direction, with the j index). The first one is the linear second order, or two points
 368 averaging

$$369 \quad \bar{\phi}^{i+1/2} = \frac{1}{2}(\phi_i + \phi_{i+1}), \quad (26)$$

370 and the second is the WENO reconstruction

$$371 \quad I_{i+1/2}[\phi^*, U] = U \sum_{s \in S} c_s \phi_{i+s}^*, \quad (27)$$

372 where S is the stencil of the reconstruction and c_s are the weights. In this paper we use
 373 n -order WENO reconstructions (Jiang & Shu, 1996; Shu, 1999), $n \in \{1, 3, 5\}$, whose
 374 stencils have n elements. The $n = 1$ case is the first order upwind interpolation and

we have either $c_0 = 1$ if $U > 0$, or $c_1 = 1$ if $U < 0$. In the $n = 3, 5$ cases the reconstruction is nonlinear because the weights c_s depend on $\{\phi_{i+s}, s \in S\}$. In any case $\sum_{s \in S} c_s = 1$. Having an even number of points, the stencils are shifted in the upwind direction, which depends on the sign of U . In the 5th order case, $S = \{-2, -1, 0, 1, 2\}$ if $U > 0$, and $S = \{-1, 0, 1, 2, 3\}$ if $U < 0$. As defined, the interpolation operators use quantities discretized at integer locations (ϕ_{i+s}) to estimate it at $i+1/2$. The reverse is also needed: use quantities discretized at half integer locations to estimate it at i . In that case we would write either $\bar{\phi}^i$ or $I_i[\phi^*; U]$. Note that (27) assumes that U is discretized at the location where ϕ^* is reconstructed. This will always be the case. For sake of completeness the WENO reconstruction is detailed in the appendix. Note that (27) is referred as a *reconstruction* rather than an *interpolation*. Reconstruction is the word used when the quantity to be interpolated is a *finite volume* quantity, and interpolation is usually reserved when the interpolated quantity is the density (e.g. h or ω), or equivalently the finite difference quantity. In this paper, the WENO scheme is applied to h^* and ω^* , the finite volume quantities. We therefore exclusively use the WENO reconstruction.

With these notations defined, we can now give the discretized model equations. They read

$$U = u/e_1^2, \quad V = v/e_2^2, \quad B = g(b + h^*/A) + k, \quad (28)$$

$$\nabla B \rightarrow (\delta_{i+1/2}[B], \delta_{j+1/2}[B]) \quad (29)$$

$$\nabla \cdot (h^* \mathbf{U}) \rightarrow \delta_i[I_{i+1/2}[h^*, U]] + \delta_j[I_{j+1/2}[h^*, V]] \quad (30)$$

$$\omega^* = f^* + \nabla \times \mathbf{u} \rightarrow f^* + \delta_{i+1/2}[v] - \delta_{j+1/2}[u] \quad (31)$$

$$k = \frac{1}{2} \mathbf{u} \cdot \mathbf{U} \rightarrow \frac{1}{2} (\overline{uU^i} + \overline{vV^j}) \quad (32)$$

$$\omega^* \mathbf{U}^\perp \rightarrow (I_j[\omega^*, V_m], -I_i[\omega^*, U_m]) \quad (33)$$

and

$$U_m = \overline{U^i}^{j+1/2}, \quad V_m = \overline{V^j}^{i+1/2}. \quad (34)$$

The only place where the metric terms are used is in (28). The required metric terms are (e_1, e_2) , the edge lengths of the dual, at respectively u-points and v-points, and A the primal cell area. In addition, and only during the initialization, A_v , the dual cell area, is needed to define $f^* = A_v f$.

Because of the rotation, the components of $\mathbf{U}^\perp = (-V, U)$ must be deduced from \mathbf{U} through some averaging because U and V are discretized at $(i + 1/2, j)$ and $(i, j +$

407 1/2) whereas \mathbf{U}^\perp requires flipped locations. This is done with the four points averag-
 408 ing in (34). This averaging is one of the decisive ingredient of the TRISK discretization
 409 (Thuburn et al., 2009; Ringler et al., 2010).

410 The discretization (33) is the main originality of this paper. The WENO reconstruc-
 411 tion is usually applied on conservation laws written in flux form. In the case of the mo-
 412 mentum equation this is on the flux of momentum. Here, because of the vector invari-
 413 ant form, there is no momentum flux. But, as discussed earlier the nonlinear Coriolis term
 414 is the vorticity flux and, as such, it can be computed with a WENO reconstruction.

415 The idea of putting some kind of upwinding and monotonicity on the nonlinear Cori-
 416 olis term is not new. In some aspect, the anticipated PV method (APVM) (Sadourny
 417 & Basdevant, 1985) implements it, although in a quite different fashion. APVM has been
 418 compared to other sub-grid closures (Graham & Ringler, 2013) in the context of RSW
 419 models. The APVM consists in expliciting the PV in the vorticity term ($\omega = qh$) and
 420 in using a first order upwind interpolation of the PV in the local direction of the flow.
 421 In the APVM there is no directional splitting. The APVM can be seen as a semi-lagrangian
 422 method where the PV is estimated at the place where it was a time step earlier. As be-
 423 ing a first order interpolation, the APVM induces more enstrophy dissipation than the
 424 method presented in this paper, while being energy-conserving. Also, contrary to our method
 425 that is parameter free, the original APVM introduces a numerical parameter that must
 426 be tuned with respect to the grid size and time step. A parameter-free extension of the
 427 APVM has been proposed (Chen et al., 2011) for the small h deviations case, whose as-
 428 sumption our method does not require. Finally, the use of the finite volume ω^* makes
 429 the APVM completely unnatural within the framework we propose. Indeed, it would re-
 430 quire to write $\omega^* \mathbf{U}^\perp$ as $q(h^* \mathbf{U}^\perp)$. We would then use a centered discretization for the
 431 mass flux $h^* \mathbf{U}^\perp$ and have the upwinding on the q term. This would completely break
 432 the symmetry of treatment between the continuity and the momentum equation. With
 433 this in mind, the discretization we propose appears oppositely quite natural, almost as
 434 self emerging from the equations, without ad-hoc choice and parameter-free.

435 For the kinetic energy term we use (32), which is a classical discretization. How-
 436 ever, it is worth noting that the kinetic energy term could also be discretized with a WENO
 437 reconstruction, as follows

$$438 \quad \overline{uU}^i + \overline{vV}^j \rightarrow s_u I_i[uU, s_u] + s_v I_j[vV, s_v] \quad (35)$$

439 with $s_u = \text{sign}(\bar{U}^i)$ and $s_v = \text{sign}(\bar{V}^j)$ inside the operator, to keep track of the up-
 440 winding directions at the grid center, and as prefactors, to ensure positivity even if $s_u <$
 441 0 or $s_v < 0$. Doing so would seriously increase the number of FLOP per time iteration
 442 (see Section 4). Given the lack of obvious immediate benefit, we did not pursue this idea
 443 further.

444 The use of WENO for the kinetic energy term may look surprising, at least for the
 445 reader not familiar with the differential geometry. The differential geometry identifies
 446 the spatial derivative in the flow direction of a quantity as the Lie derivative of its as-
 447 sociated differential form (Frankel, 2011). The Cartan identity splits the Lie derivative
 448 in two terms, each one participating to the transport in a very specific way. For the mo-
 449 mentum, the associated differential form is \mathbf{u} , and these two terms are the nonlinear Cori-
 450 olis term and the gradient of kinetic energy of the vector-invariant form. Each term can
 451 be seen as a composition of two basic operations of the differential geometry: the exte-
 452 rior derivative and the interior product, respectively a generalization of the ∇ operator,
 453 and of the inner product. In the discretized equations we presented, the exterior deriva-
 454 tive shows up as the finite difference operators $\delta_i[\cdot]$ and $\delta_j[\cdot]$, whereas the interior prod-
 455 uct shows up as the WENO reconstruction operators $I_i[\cdot]$ and $I_j[\cdot]$. The idea of using
 456 Cartan identity to discretize the transport of a vector field was pioneered by Mullen et
 457 al. (2011), who also showed that a WENO reconstruction improves the accuracy, com-
 458 pared to the upwind first order reconstruction. Here we somehow generalize these results
 459 to the full RSW equations.

460 3.2 Time stepping

461 The code clearly separates the time scheme in one generic module. The implemen-
 462 tation of a time scheme is very close to a textbook presentation. This is made possible
 463 because space and time discretizations are independent. The model variables are split
 464 into two groups: the prognostic variables $\phi = (u, v, h^*)$, obeying an explicit time evo-
 465 lution equation, and the diagnostic variables $\Phi = (\zeta^*, U, V, p)$. Formally, the code han-
 466 dles $s = (\phi, \Phi)$ the model state, as a collection of all variables, that obeys $\partial s / \partial t = \mathbf{L}(s)$,
 467 with \mathbf{L} the model operator. To better expose the prognostic and the diagnostic parts \mathbf{L}

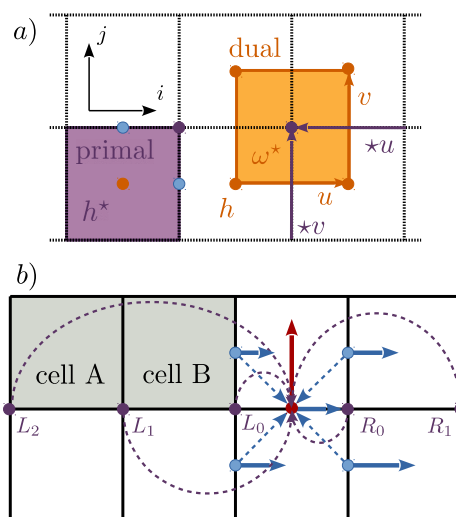


Figure 1. a) The classical C-staggering with locations for scalars (orange circles), vector components (blue circles) and vorticity (purple circles). The features (vertices, edges, faces) are colored in purple for the primal grid and orange for the dual grid. b) Illustration of the vorticity unwinding. Away from the boundaries, the vorticity flux (red arrow) at the v -point (red circle) is computed as the product of U (blue arrow), interpolated with a four points averaging (dotted blue arrows), and ω^* reconstructed along i using the five points stencil (L_2, L_1, L_0, R_0, R_1). If cell A is masked, the stencil is shortened (L_1, L_0, R_0); if both cell A and cell B are masked, the stencil is (L_0). In that latter case, if U were to the left, the vorticity would be reconstructed with the stencil (R_1, R_0, L_0).

468 can be expanded into

$$469 \quad \frac{\partial \phi}{\partial t} = \mathbf{R}[\phi, \Phi] \quad (36)$$

$$470 \quad \Phi = \mathbf{D}[\phi], \quad (37)$$

471 with \mathbf{R} the right hand side for the prognostic variables and \mathbf{D} the diagnostic relations for
 472 Φ . Currently the code proposes two time schemes: the Leap-Frog Adams Moulton scheme
 473 (LFAM3) (Shchepetkin & McWilliams, 2005) and the 3rd order stably strongly preserv-
 474 ing Runge Kutta scheme (Gottlieb et al., 2001) (RK3)

$$475 \quad s^{(1)} = s^n + \Delta t \mathbf{L}[s^n] \quad (38)$$

$$476 \quad s^{(2)} = s^n + \frac{1}{4} \Delta t (\mathbf{L}[s^n] + \mathbf{L}[s^{(1)}]) \quad (39)$$

$$477 \quad s^{n+1} = s^n + \frac{1}{6} \Delta t (\mathbf{L}[s^n] + \mathbf{L}[s^{(1)}] + 4 \mathbf{L}[s^{(2)}]), \quad (40)$$

478 where Δt is the time step and s^k the model state at time step k . Both are third order
 479 in time. The LFAM3 is a predictor corrector scheme with only two calls to the right-hand
 480 side L per time iteration, whereas RK3 requires three calls to the right-hand side. RK3
 481 is the model default choice.

482 **3.3 Boundary conditions at lateral boundaries**

483 RSW models are quite often tested either in bi-periodic domains or on the whole
 484 sphere, more rarely in domains with lateral boundaries. For oceanic applications, han-
 485 dling the lateral boundaries is a necessity. The other reason to present the lateral bound-
 486 ary conditions is that they fit particularly well with the choice of upwinding the vortic-
 487 ity in the nonlinear Coriolis term. The no-flow is enforced at no cost thanks to the C-
 488 grid but interestingly, the free-slip and the no-slip boundary conditions appears very nat-
 489 urally as conditions on the vorticity, which directly impact the normal component of flux
 490 of vorticity at the boundary.

491 Solid boundaries can be either at the domain boundary or inside the domain. For
 492 the latter case, we use a mask system $m_{i,j}$. A cell (of the primal grid) is solid if $m_{i,j} =$
 493 0, fluid if $m_{i,j} = 1$. The no-flow boundary condition is imposed at each edge of the pri-
 494 mal grid where one adjacent cell is solid. It simply consists in setting $u = 0$ or $v = 0$
 495 at this edge. This is the standard technique. The real point of attention is on defining
 496 ζ^* at points sitting along the boundary. The curl expression (31) cannot be immediately
 497 used because the dual cell is not fully fluid. However, ζ^* conserves its physical mean-
 498 ing of being both the amount of vorticity in this partial cell, and the circulation along
 499 the boundary of this partial cell. The latter offers the natural way to define ζ^* , which
 500 completely depends on the slip condition. In the free-slip case, $\zeta^* = 0$ at points along
 501 the boundary. In the no-slip case, we keep compute ζ^* with (31) but we set $u = 0$ and
 502 $v = 0$ for all edges, not fully in the fluid. For a straight boundary, say along i at $j =$
 503 0 and the fluid being for $j > 0$, this definition yields $\zeta_{i,0}^* = -u_{i,1/2}$, which expresses
 504 that a right-going flow generates a negative vorticity. The use of the differential forms
 505 remove, once again, all the metric terms from the relation. The no-slip boundary con-
 506 dition behaves as a source of vorticity localized at the boundary. Interestingly, once this
 507 vorticity is generated, it might be transported into the fluid by the nonlinear Coriolis
 508 term. Let us see how.

509 For cell edges close to the boundary, the five points stencil of the the WENO 5th
 510 does not fit in. To overcome this issue, the code implements a varying stencil width with
 511 the following policy: use the widest biased stencil, i.e. either one, three or five points,
 512 fitting within the fluid cells. The one point stencil is the upwind first order interpola-
 513 tion. For the three points stencil, we use the third order WENO reconstruction (Shu,
 514 1999) (explicated in Appendix A). The consequence is that the outward vorticity flux
 515 at the edge next to the boundary is computed with a first upwind scheme, that adds a
 516 little bit more of dissipation. In the free-slip case, since $\zeta^* = 0$ at the boundary there
 517 is no outward flux.

518 Instead of imposing the velocity at the boundary, and therefore the vorticity, we
 519 may want to impose the normal stress. In that case, it requires to introduce a viscos-
 520 ity to relate the stress to the velocity. We did not pursue this idea further as it is be-
 521 yond the scope of the paper.

522 4 Speed

523 4.1 Implementation choices

524 Performances on both the quality of the solutions and the speed were the top pri-
 525 orities in the code design. To achieve speed, a compiled language is required. Until re-
 526 cently this imposed the use of Fortran or C or a blend of Python and C (Pressel et al.,
 527 2015). The Julia language is currently used on several projects (Ramadhan et al., 2020;
 528 Klöwer et al., 2020), whose chief advantage is to be a compiled language. Here we chose
 529 another route. The code is entirely written in Python, without sacrificing speed. This
 530 is possible thanks to the numba module. Numba (Lam et al., 2015) uses the LLVM com-
 531 piler (Lattner & Adve, 2004) to compile Python code. The bulk of the code is interpreted
 532 Python, but all the computational functions are compiled. In practice, to compile a func-
 533 tion amounts in specifying its signature, namely the types of its inputs and outputs. In-
 534 side a function, and contrary to the pythonic policy, the loops can be explicitly devel-
 535 oped ; the compiler takes care of them. Note that since Julia’s compiler is also LLVM,
 536 it makes the use of Julia less decisive for HPC.

537 The second element of speed is to systematically duplicate all arrays. Arrays are
 538 thus stored in $[k, j, i]$ and in $[k, i, j]$ conventions, the k index being for the layer in-
 539 dex. The motivation is to always do finite differences with the convention where the data

540 are contiguous in memory. Thus, the computation of the spatial derivative $\partial/\partial j$ or of
 541 the along j -interpolation is done with the [k,i,j] convention. Data contiguity allows
 542 a better usage of the L1-cache, which is the fastest. The price of duplicating is to per-
 543 form transpose operations to exchange the data from one convention to the other. For-
 544 tunately, the transpose operation is very fast as it is highly optimized. In practice the
 545 transpose operation is done 20 times per time stage, which represents 16% of the total
 546 time. Another advantage of this approach is to easily guarantee the numerical isotropy.
 547 The two directions i and j are treated absolutely equivalently because there is only one
 548 function for both operations. This is particularly convenient for the WENO reconstruc-
 549 tion. The WENO reconstruction, even though requiring many more operations than the
 550 linear interpolation, is not much slower.

551 A third element of speed is of course the use of the covariant equations with the
 552 index coordinates that turn spatial differentiations into subtractions. The number of mul-
 553 tiplications is minimal. The only computation involving many multiplications is the WENO
 554 reconstruction.

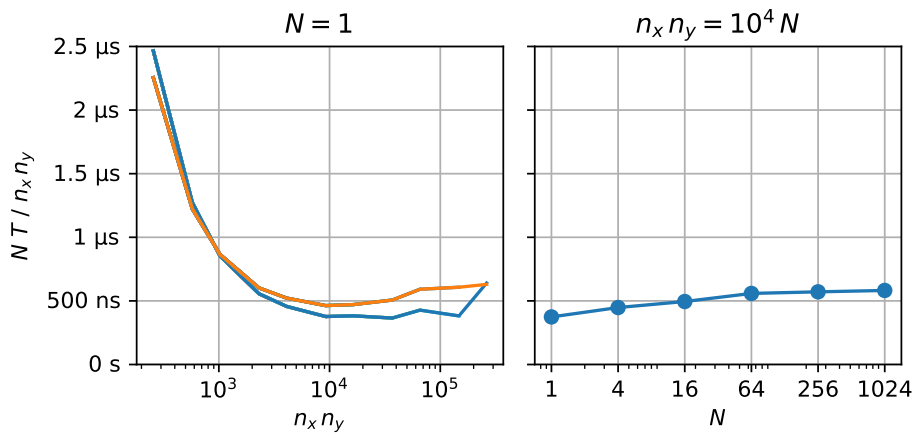


Figure 2. Walltime per time iteration T rescaled with $N/(n_x n_y)$. On the left for the mono-
 core case as a function of the domain size $n_x n_y$ and on the right the weak scaling, where the
 number of cores N is increased from $N=1$ up to $N=1024$, while the domain size per core
 $n_x n_y=10^4$ is kept constant. In blue are the performances for the supercomputer and in orange for
 a notebook (see text for the CPU specs).

555 **4.2 Speed assessment**

556 With these choices, the code (Roulet, 2021) is very fast. With the default 5th or-
 557 der WENO, and the SSP-RK3 time scheme, the code speed is about 0.3 μs per iteration
 558 per grid point (Figure 2). The performances have been measured on a notebook (Intel[®]
 559 Core[™] i7-6600U at 2.6GHz) and Rome (AMD[®] EPYC 7502 at 2.5GHz) a supercom-
 560 puter hosted at TGCC (Saclay, France). Timing has been averaged over thousand time
 561 iterations and excludes the I/O. The code has an almost perfect weak scaling (Figure 2b).
 562 We may wonder how close is the code speed to the peak CPU performances. To answer
 563 it we need to determine how many floating operations are done per grid cell and per time
 564 iteration.

565 To estimate how far this speed is from the maximum peak performance of the CPU,
 566 we count all the floating point operations (Table 1). The current implementation uses
 567 840 Flop per time step and per grid point. With the minimum time $T = 400 ns$ on the
 568 Rome supercomputer, this gives 2.1 GFlop s^{-1} , which corresponds to 84% of the CPU
 569 clock frequency. It is not overstated to say that this implementation is close to the max-
 570 imum hardware limits. Interestingly, with 708 Flop, the WENO reconstruction is the ma-
 571 jor contributor, representing 84% of the total Flop. By using a linear interpolation (up-
 572 wind 5th), the reconstruction involves only 108 Flop¹ and therefore only 240 Flop per
 573 time step. Naively we could expect the code to be 840:240=3.5 time faster. This is not
 574 the case. In practice the linear interpolation gives $T \approx 350 ns$ corresponding to 0.7 GFlop s^{-1} .
 575 The reason is clear. In this case the code speed is limited by the memory access, which
 576 makes the CPU waiting for data. By increasing the arithmetic intensity, the use of WENO
 577 puts the code into the compute-bound region, which maximizes the Flop per second.

578 **5 Accuracy**

579 The merits of the numerical choices are tested with three experiments, each test-
 580 ing one aspect: the merging of two vortices, the interaction of a dipole in an elliptical
 581 domain with free and no-slip condition, a dam break experiment in an annulus. The ex-
 582 periments are set in quite intense nonlinear regimes, although not going up to either shock
 583 wave formation or dry bed emergence.

¹ Corresponding to 3 stages, 2 functions, 2 directions, 5 multiplications and 4 additions.

Table 1. Number of floating operations^a breakdown

Function	Term	#M	#A
Continuity	WENO 5 th	64	54
	$d(h^* \mathbf{U})$	2	4
Vorticity flux	WENO 5 th	64	54
	\mathbf{U}^\perp	2	4
	Coriolis	2	4
	$\omega^* \mathbf{U}^\perp$	2	2
Bernoulli	grad	0	4
Diagnostics	\mathbf{U}	2	0
	ζ^*	0	3
	$\mathbf{u} \cdot \mathbf{U}/2$	3	3
	$g(h^* + h_b^*)/A$	2	1
Total per stage		143	133
SSP RK3	stage 1	1	1
	stage 2	2	2
	stage 3	3	3
Total per time step		435	405

^aFloating points operations involve multiplications (#M) and additions/subtractions (#A). The numbers are given per grid point and per call to the function. For the RK3 time stepping, which is the default, the total number per time step is the three times the total per stage plus the operations in the time scheme itself.

584 **5.1 Merging of two vortices**

585 This first set of experiments tests the sensitivity of the conservation laws on the
 586 model resolution. The experiments consist in the time evolution of two Gaussian vor-
 587 tices initially in geostrophic balance. The two vortices, of radius $\sigma = 0.07$, are sepa-
 588 rated by a distance $d = 1.4 \sigma$; specifically

589
$$h(x, y) = H + h_0 (G(x - d/2, y; \sigma) + G(x + d/2, y; \sigma)) ,$$

590 with $h_0 = 0.2$, $H = 1$ and $G(x, y; \sigma) = \exp[-(x^2 + y^2)/(2\sigma^2)]$. The domain is square,
 591 with an edge length $L = 1$. We use the free-slip boundary condition. The two physi-
 592 cal parameters are $g = 1$ and $f = 5$ which yield a Rossby deformation radius $R =$
 593 $\sqrt{gH}/f = 0.2$, that sets the vortices in the submesoscale range. The speed scale is $gh_0/(f\sigma)$,
 594 which yields a Rossby number of $Ro = gh_0/(f\sigma)^2$, namely $Ro \approx 1.6$, again typical of
 595 the submesoscale regime. The vortices are anticyclones because $h_0 > 0$. The flow is in-
 596 tegrated up to time $t = 10$. The domain is meshed with N^2 grid cells of uniform size.
 597 N is varied from $N = 100$ to $N = 3,200$, by a succession of doubling.

598 The two vortices are close enough to merge, as revealed by the presence of single
 599 core of negative PV in the center at $t = 10$ (Figure 3), instead of two initially. The de-
 600 tails of the merging sequence depend on the resolution, among which the amount of fil-
 601 aments and the balancing time. But quite clearly, and fortunately, the solution converges
 602 with increasing N . The cases $N = 1,800$ and $N = 3,200$ are almost indistinguishable
 603 by eye. A striking property is the absence of noise on the PV fields, for all resolutions.
 604 This is a consequence of the implicit dissipation and mixing provided by the MILES ap-
 605 proach. A second striking feature is the capability for the code to produce and maintain
 606 very thin filaments. Of course the case $N = 3,200$ is quite extreme for such a trivial
 607 flow but nevertheless it is worth emphasizing. Not only are the filaments thin, they can
 608 also be intense in terms of PV difference with the background state. This results in the
 609 shear instability of a few filaments, as seen on the $N = 1,800$ case.

610 To better assess the convergence with the resolution we diagnosed the cumulative
 611 global dissipation (Fig. 4a-b) for both the energy $\epsilon_E = (E_0 - E)/E_0$ and the enstro-
 612 phy $\epsilon_Z = (Z_0 - Z)/Z_0$, where the superscript 0 denotes the value at $t = 0$. The global
 613 energy E is defined as $E = \int eh^* - E_b$, with the energy density

614
$$e = \frac{1}{2} \mathbf{u} \cdot \mathbf{U} + \frac{1}{2} gh , \tag{41}$$

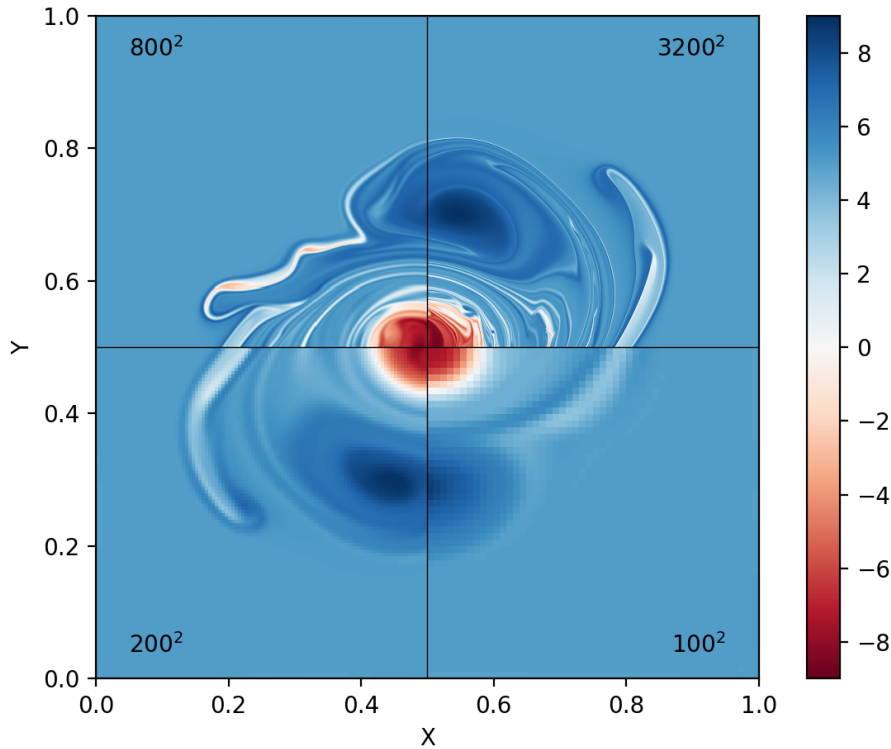


Figure 3. Snapshots of potential vorticity at $t=10$, after the vortices merged, for four resolutions $n_x n_y = 100^2, 200^2, 800^2, 3,200^2$. Only a quarter of each domain is displayed. The parameters are $g=1, H=1, f=5$. The anticyclones were initially Gaussian, in geostrophic balance, with a layer depth $h=1.3$ at their center.

615 and the background potential energy $E_b = \int (gH^2/2) dx dy$. E_b is removed from $\int eh^*$
 616 because it is the part of the energy that cannot be dissipated. This is the energy of the
 617 rest state. Still, the total amount of energy dissipated is fairly small: $\epsilon_E \sim 2\%$ for $N =$
 618 100 and $\epsilon_E \sim 4.10^{-5}$ for $N = 3,200$, which is approaching perfect conservation. The
 619 code actually reaches the point where the question becomes theoretical: during a vor-
 620 tex merging event should the energy dissipation go to zero in the limit of infinite reso-
 621 lution? The present experiments suggest that not but this would deserve a more thor-
 622 ough study, beyond the scope of this paper. The case of the enstrophy dissipation (Fig. 4b)
 623 is very different. In all cases there is a finite amount of dissipation but the increase of
 624 resolution delays the time at which the dissipation really starts, as well as it increases
 625 the equilibration time. In the $N = 100$ case, the merging process is almost completed
 626 as indicated by the plateau, at the largest resolution, there is still a lot of enstrophy to

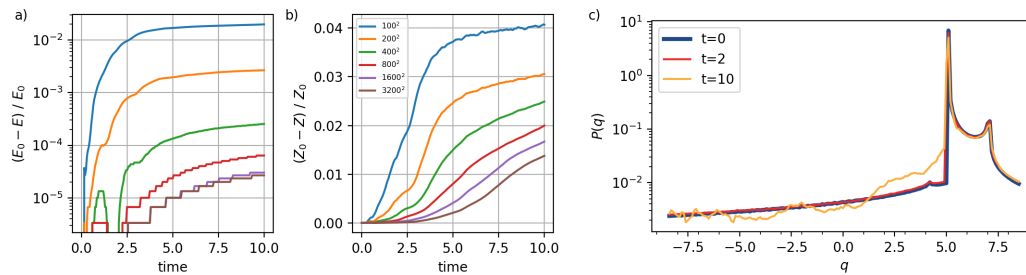


Figure 4. Energy (a) and enstrophy (b) dissipated as a function of time and resolution (color) for the vortex merging experiment. The energy of the rest state $gH^2/2$ has been removed from E and E_0 . (c) probability density function of potential vorticity at $t = 0$ (blue), $t = 2$ (red) and $t = 10$ (orange) for the merging experiment at the 3,200² resolution.

627 be dissipated. It is not clear whether all resolutions yield the same amount of enstro-
 628 phy dissipation. Again this requires a more thorough study that we postpone for a later
 629 paper.

630 Finally to assess the material conservation of PV we plot the probability density
 631 function of PV in the $N = 3,200$ case for $t = 0$, $t = 2$ and $t = 10$ (Fig. 4c). At $t = 2$
 632 the enstrophy dissipation has not yet started (Fig. 4b) meaning the flow is still inviscid,
 633 even though the vortices are already producing filaments (not shown). The pdf of PV
 634 is remarkably close to its $t = 0$ value. Material conservation is very well ensured. At
 635 $t = 10$ the pdf departs from its initial value. This is due to the mixing at the grid-scale.
 636 Interestingly the PV on the cyclonic part (the initial vortices are slightly shielded with
 637 a ring of cyclonic PV) remains quite well conserved. This confirms the visual impression
 638 of the snapshot (Fig. 3), the cyclonic PV does not filament, therefore it does not mix,
 639 therefore its pdf should remain constant in time, as it does.

640 5.2 Vortex-wall interaction

641 In this set of experiments we test how the code performs on handling boundary con-
 642 ditions. The experiments consist in the time evolution of a vortex dipole with either the
 643 free-slip or the no-slip boundary condition (Figure 5). In order to have a variety of bound-
 644 ary shapes at the grid scale, the domain is elliptical, whose major and minor axis lengths
 645 are respectively 2 and 1. The grid is 1,600×800 with square grid cells. The experiments
 646 are started at $t = 0$ with two Gaussian vortices initially in geostrophic balance at the

647 center of the domain. The two vortices, of radius $\sigma = 0.1$, are separated by a distance
 648 $d = 1.1 \sigma$; specifically

649
$$h(x, y) = H + h_0 (G(x - d/2, y; \sigma) - G(x + d/2, y; \sigma)) ,$$

650 with $h_0 = 0.15$ and $H = 1$. The two physical parameters are $g = 1$ and $f = 5$.

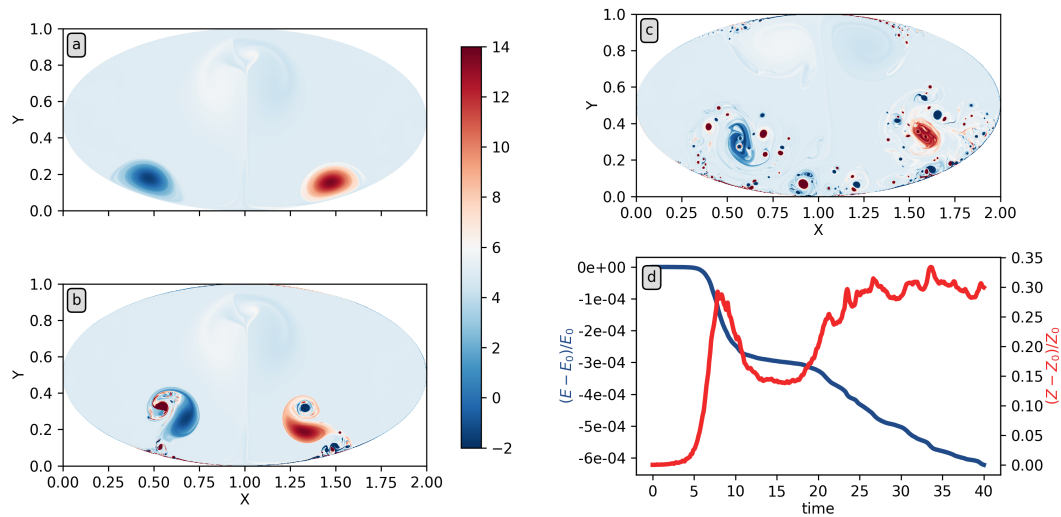


Figure 5. Potential vorticity snapshots of the dipole-wall interaction in the free-slip case at $t = 12$ (a) and no-slip case at $t = 12$ (b) and $t = 40$ (c). (d) Evolution of the energy and the enstrophy in the no-slip case. The resolution is $1,600 \times 800$. The initial position of the dipole center is at $(1, 0.5)$.

651 In either cases, the dipole starts to move along the minor axis Southward, while
 652 a weak trail of opposite PV, due to the vortex shield, moves Northward. As the dipole
 653 approaches the wall, the dynamics starts to differ between the free-slip and the no-slip
 654 boundary conditions. In the free-slip case, the dipole splits and each vortex continues
 655 its journey, following the wall, in an inviscid manner, according to the mirror rule (Fig. 5a).
 656 The PV remains materially well conserved, even close to the boundary. In particular there
 657 is no spurious source or sink of PV near the wall. The no-slip case differs dramatically
 658 (Fig. 5b). The phenomenology is well documented even though it is usually studied in
 659 the context of the two dimensional Euler equations (Keetels et al., 2007; Farge et al., 2011).
 660 The dipole generates a thin ribbon of opposite PV along the wall. As the dipole splits,
 661 this ribbon detaches from the wall and gets entrained in the domain where it wraps around
 662 each vortex. This halts the vortex drift along the wall. Instead, the vortices describe a

663 loop and hit the wall again, generating another ribbon of PV that is later detached. The
 664 rebonds continue causing the initial vortices to remain trapped near the collision point.
 665 The series of layer detachments seed the flow with PV ribbons. The ribbons width and
 666 the magnitude of their vorticity depend on the numerical resolution. For this experiment,
 667 the ribbons are strong enough to experience shear instability causing them to roll up into
 668 small vortices. The domain is thus progressively filled with a swarm of small scales vor-
 669 tices (Fig. 5c). The dipole-wall interaction is fundamentally dissipative. It dissipates en-
 670 ergy but it creates enstrophy (Fig. 5d). After the first collision ($t = 8$), the dissipated
 671 energy $(E_0 - E)/E_0 \approx 3 \cdot 10^{-4}$, whereas the created enstrophy $(Z - Z_0)/Z_0 \approx 30\%$.
 672 During the following collisions, the dissipated energy increases steadily up to $6 \cdot 10^{-4}$ at
 673 $t = 40$. The enstrophy behaves differently: it globally increases with time but with os-
 674 cillations. As the PV distribution becomes more and more random, the amount of cre-
 675 ated enstrophy plateaus at roughly 30%. In comparison, in the free slip case and at $t =$
 676 40, $(E_0 - E)/E_0 \approx 3 \cdot 10^{-6}$, and $(Z - Z_0)/Z_0 \approx -2 \cdot 10^{-3}$, which again shows the code
 677 ability to preserve global invariants, even though the numerics has a build-in mechanism
 678 for dissipation.

679 The solution at $t = 40$ has become quite turbulent (Fig. 5c), suggesting a fairly
 680 large Reynolds number. Determining the Reynolds number is a challenging task because
 681 there is no explicit viscosity in the model. The dissipation is solely handled by the WENO
 682 reconstructions, in a highly implicit manner. This is a classical issue with the implicit
 683 approach (Zhou et al., 2014). A possibility is to diagnose an effective numerical viscos-
 684 ity $\nu = Z^{-1} dE/dt$, based on the fact that for a true viscous operator the energy dis-
 685 sipation rate is related to Z by $dE/dt = -\nu Z$. From this numerical viscosity we can
 686 form an equivalent Reynolds number $Re = E^{1/2}/(H\nu)$. With this metric, the Reynolds
 687 number at $t = 40$ is $Re \sim 3 \cdot 10^9$.

688 5.3 Dam-break problem

689 In this last experiment we focus on the gravity waves dynamics, and its relation
 690 with the PV, on a dam-break experiment. To illustrate the code ability to handle curved
 691 coordinates we use an annulus domain with inner radius $r_0 = 1$ and outer radius $r_1 =$
 692 2. The coordinates (i, j) represent respectively the radial and the orthoradial directions.
 693 The metric tensor reads $\mathbf{g} = \text{diag}(dr^2, r^2 d\theta^2)$, where dr and $r d\theta$ are the grid lengths
 694 in the i and j direction. The discretization is uniform in dr and $d\theta$, with respectively

695 and 200 grid points in i and 1,600 in j . The initial state is $h = H + h_0 \tanh(y/\sigma)$ and
 696 $\mathbf{u} = 0$, with $y = r \sin \theta$, $h_0 = 0.15$, $H = 1$ and $\sigma = 0.05$. The two physical parameters are $g = 1$ and $f = 5$. The imbalance at $t = 0$ generates inertia-gravity waves and

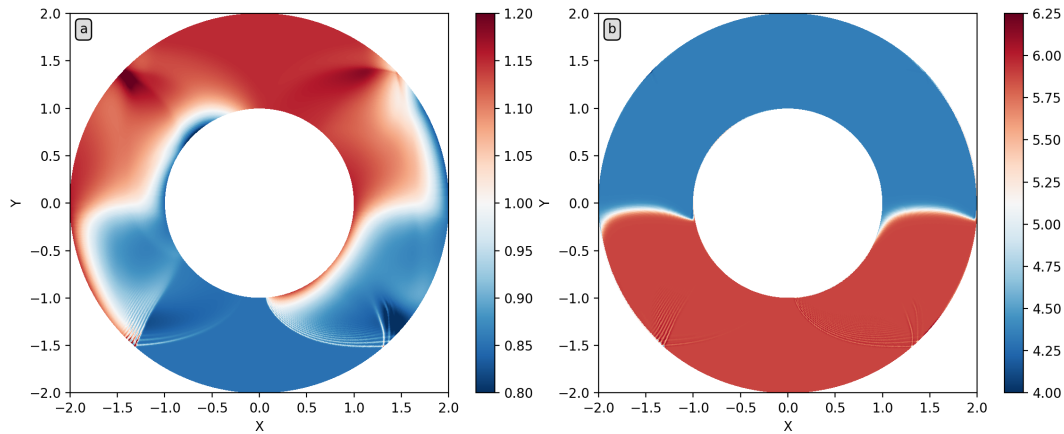


Figure 6. Snapshot of layer depth (a) and potential vorticity (b) at $t=1.5$ resulting from a dam-break located along $y=0$, with amplitude $\Delta h=0.3$. The other parameters are $g=H=1$ and $f=5$. Cylindrical coordinates are used to define the model metric. The resolution is $200 \times 1,600$.

697
 698 four Kelvin waves, two along each boundary. The Kelvin waves have a clear signature
 699 on h (Fig. 6a), propagating along the boundaries with the boundary on their right (be-
 700 cause $f > 0$), with a trapping width consistent with $R_d = 0.1$. Their propagation speed
 701 is close to $c = \sqrt{gH} = 1$ as a visual estimate tells: at $t = 1.5$ the Kelvin waves prop-
 702 agating along the inner boundary have moved of roughly a quarter turn. The agreement
 703 is not perfect because the regime is nonlinear enough, introducing nonlinear corrections
 704 in the wave speed. The structure of the inertia-gravity waves is more complicated. There
 705 is a net asymmetry between the waves propagating on the shallower part $H - h_0$ and
 706 the deeper part $H + h_0$. On the shallower part, the waves have clear nonlinear effects,
 707 as revealed by the series of small scales ripples and suggestive of shock wave dynamics.
 708 As there is no particular numerical treatment to handle the correct dissipation at shocks,
 709 there is no warranty that these ripples should be there, although they might be solitons.
 710 Having such small scales patterns on h is really due to the 5th order WENO reconstruc-
 711 tion on the mass flux. Switching to a first order interpolation removes all these signals
 712 and makes h very smooth.

713 In contrast, the PV field has a very simple structure (Fig. 6b). At $t = 1.5$, the
 714 geostrophic currents, resulting from the geostrophic adjustment and localized along the
 715 initial discontinuity, have started to transport PV. This is the reason for the PV jump
 716 to be deformed near the boundaries. The PV field is remarkably free of any wave sig-
 717 nal, except at the shock waves places where the PV exhibits the same ripples structure
 718 than the wave. These ripples are indicative of dissipation in action, breaking the invis-
 719 cid assumption and the material conservation. Interestingly these PV ripples propagate
 720 with the waves so that their rectifying effect on the PV is much smaller. With this col-
 721 orscale the net effect is invisible but a magnified colorscale reveals thin striations at few
 722 places. These small amplitude striations are the clear evidence that dissipation occurred
 723 which yielded local creation and destruction of PV. We will not go into more details as
 724 the study of wave-PV coupling is far beyond the scope of this paper. However we be-
 725 lieve the numeric we propose is very promising to study these questions.

726 6 Conclusions

727 In this paper we have presented a fast and accurate discretization for the RSW equa-
 728 tions. Accuracy, measured in terms of potential vorticity dynamics and conservation laws,
 729 is achieved by adapting the MILES approach (Boris et al., 1992) to the vector-invariant
 730 form of the RSW equations. The decisive step is to use a 5th order WENO reconstruc-
 731 tion on both the mass flux and the nonlinear Coriolis term. Currently the method re-
 732 quires a logically rectangular C-grid. The generalization to the cubed sphere is possi-
 733 ble, the difficulty lays in handling the vorticity interpolation at the grid cells next the
 734 cube edges. The generalization to hexagonal grids is more challenging because the vor-
 735 ticity points are not immediately aligned with \mathbf{U}^\perp , but the recent developments on WENO
 736 reconstructions for unstructured grids (Tsoutsanis et al., 2011) pave the way to a clean
 737 solution. Speed is achieved with a series of choices rather than a single recipe, yet with
 738 a pure Python code. Though not the main point of this paper, we clearly proved that
 739 Python has become a serious option for HPC, rivaling with Fortran. In the perspective
 740 of using trained neural networks as parameterization for models, having a kernel in Python
 741 is an advantage. The code reaches typically 2 GFlop per second per core on a classical
 742 CPU architecture, which is above half the theoretical peak performance. The choices are:
 743 a reformulation of the continuous equations, the use of the Numba module to compile
 744 the most demanding functions, and the duplication of all arrays in two memory layouts

745 to increase the arithmetic intensity by ensuring data contiguity in all functions. The re-
 746 formulation is based on the introduction of h^* and ω^* , the finite volume version of h and
 747 the vorticity ω ; the use of index coordinates (i, j) ; and the introduction of \mathbf{u} and \mathbf{U} ,
 748 respectively, the covariant and the contravariant velocity. The grid lengths are used at
 749 only two places, to compute \mathbf{U} from \mathbf{u} with the metric tensor \mathbf{g} , and to relate h to h^* .
 750 Everywhere else grid lengths are gone. Finite differences boil down to subtractions with
 751 no multiplication or division, which reduces the number of Flop and the amount of data
 752 transferred between the CPU and the memory.

753 With these choices, the floating points operations associated with the WENO re-
 754 constructions represent 85% of the total number of operations and, thanks to data con-
 755 tiguity, these operations are done at the CPU clock frequency, without being penalized
 756 by memory access. This particular combination of a large fraction of the total Flop with
 757 the data available in the fastest L1 cache is responsible for the overall code speed.

758 From the physical point of view, the numerical solutions show remarkable prop-
 759 erties: the PV field does not exhibit any noise at the grid scale, the material conserva-
 760 tion is excellent as far as the flow does not require enstrophy dissipation. The energy dis-
 761 sipation is vanishingly small with increasing resolution, even in the case where a finite
 762 amount of enstrophy is dissipated. The code handles arbitrary shaped domains with both
 763 free-slip and no-slip condition. The boundary condition on momentum is done quite nat-
 764 urally through the definition of the vorticity along the boundary, which is used to esti-
 765 mate the nonlinear Coriolis term. The no-slip boundary condition generates enstrophy,
 766 as expected, whereas it dissipates energy. In that case, by interacting with the bound-
 767 ary, an initially smooth PV field continuously develops fine scale structures, causing the
 768 flow to become turbulent. Finally we have shown on a dam-break experiment that the
 769 PV field remains very smooth even when small scale waves propagate. The build-in nu-
 770 merical dissipation allows the code to handle shock waves without blow-up even though
 771 it remains to be proven that this implicit dissipation satisfies the proper entropy con-
 772 dition on shock waves.

773 This paper has shown a new way of implementing the MILES approach in a RSW
 774 model. Several generalizations can be contemplated, some of them already mentioned
 775 earlier, but the real generalization is to adapt this idea to the full three dimensional equa-
 776 tions, in the non-hydrostatic regime. The extension is simple: use the WENO reconstruc-

777 tion to each sub-term of the vortex-force term. The hope is that it provides enough build-
 778 in dissipation to handle the direct cascades of both enstrophy and energy, and it acts as
 779 a substitute for an explicit subgrid-scale closure. This idea has already been turned in
 780 a real LES code, that shows comparable performances to the code presented in this pa-
 781 per.

782 **Appendix A WENO reconstruction**

783 We now specify the $I_{i+1/2}[\phi, U]$ operator, that computes the flux $U\phi$ at location
 784 $i+1/2$. Because the operator is applied to finite volume quantities exclusively, it is strictly
 785 speaking a *reconstruction*, rather than an *interpolation*. We use the original WENO re-
 786 construction (Jiang & Shu, 1996; Shu, 1999), also denoted WENO-JS. We express it in
 787 terms of Legendre polynomial (Balsara et al., 2016). We assume without loss of gener-
 788 ality $U > 0$ and we start with the fifth order case, which is the general case.

789 **A1 5th order case**

790 The fifth order reconstruction is based on the three stencils $S_1 = \{i-2, i-1, i\}$,
 791 $S_2 = \{i-1, i, i+1\}$ and $S_3 = \{i, i+1, i+2\}$ relative to cell index i . The reconstruction
 792 reads

793
$$I_{i+1/2}[\phi, U] = U (w_1\tilde{\phi}_1 + w_2\tilde{\phi}_2 + w_3\tilde{\phi}_3) \tag{A1}$$

794 with

795
$$\tilde{\phi}_k = \phi_i + \phi_k^{(1)} P_1(1/2) + \phi_k^{(2)} P_2(1/2), \tag{A2}$$

796
$$w_k = \frac{\alpha_k}{\alpha_1 + \alpha_2 + \alpha_3} \quad \text{and} \quad \alpha_k = \frac{\gamma_k}{(\beta_k + \epsilon)^2} \tag{A3}$$

797 where $P_1(x) = x$, $P_2(x) = x^2/2 - 1/24$ are the Legendre polynomials on the $[-1/2, 1/2]$
 798 interval, and w_k are the nonlinear weights associated with the stencils S_k . The discretiza-
 799 tion is completed with the definitions of the smoothness indicator
 800

801
$$\beta_k = \left(\phi_k^{(1)}\right)^2 + \frac{13}{12} \left(\phi_k^{(2)}\right)^2, \tag{A4}$$

802 the value of first $(\phi_k^{(1)})$ and second $(\phi_k^{(2)})$ moments associated with the stencil S_k

803
$$\phi_1^{(1)} = (\phi_{i-2} - 4\phi_{i-1} + 3\phi_i)/2 \quad \text{and} \quad \phi_1^{(2)} = (\phi_{i-2} - 2\phi_{i-1} + \phi_i), \tag{A5}$$

804
$$\phi_2^{(1)} = (-\phi_{i-1} + \phi_{i+1})/2 \quad \text{and} \quad \phi_2^{(2)} = (\phi_{i-1} - 2\phi_i + \phi_{i+1}), \tag{A6}$$

805
$$\phi_3^{(1)} = (-3\phi_i + 4\phi_{i+1} - \phi_{i+2})/2 \quad \text{and} \quad \phi_3^{(2)} = (\phi_i - 2\phi_{i+1} + \phi_{i+2}), \tag{A7}$$

806 and the linear weights

$$807 \quad \gamma_1 = 1/10, \quad \gamma_2 = 3/5, \quad \gamma_3 = 3/10. \quad (\text{A8})$$

808 The regularization factor is set to $\epsilon = 10^{-8}$. These linear weights are the original ones
 809 proposed by Shu. They are the ones that makes the whole reconstruction fifth order at
 810 locations where ϕ is smooth.

811 The adaptation of this reconstruction to the case of the vorticity, namely $I_i[\omega, V]$,
 812 is straightforward. Because of the vorticity being discretized at half integers indices, the
 813 only change is to replace the ϕ_i terms with $\omega_{i-1/2}$ in the above formulas.

814 Close to boundary we use a 3rd order WENO reconstruction (Shu, 1999), if either
 815 $\{i-2\}$ or $\{i+2\}$ is outside of the domain but the $\{i-1, i, i+1\}$ cells are inside the do-
 816 main. We downgrade to the 1st order reconstruction if either $\{i-1\}$ or $\{i+1\}$ is out-
 817 side the domain. For sake of completeness we explicit the formula in these two cases.

818 **A2 3rd and 1st order cases**

819 The third order case (Shu, 1999) reads

$$820 \quad I_{i+1/2}[\phi, U] = U (w_1 \tilde{\phi}_1 + w_2 \tilde{\phi}_2) \quad (\text{A9})$$

821 with $\tilde{\phi}_k = \phi_i + \phi_k^{(1)} P_1(1/2)$,

$$822 \quad w_k = \frac{\alpha_k}{\alpha_1 + \alpha_2}, \quad \alpha_k = \frac{\gamma_k}{(\beta_k + \epsilon)^2}, \quad \beta_k = \left(\phi_k^{(1)}\right)^2, \quad (\text{A10})$$

823
 824 $\gamma_1 = 1/3, \gamma_2 = 2/3, \phi_1^{(1)} = \phi_i - \phi_{i-1}$ and $\phi_2^{(1)} = \phi_{i+1} - \phi_i$.

825 The first order case is simply

$$826 \quad I_{i+1/2}[\phi, U] = U \phi_i. \quad (\text{A11})$$

827 **Acknowledgments**

828 This work was supported by the French National program LEFE (Les Enveloppes Flu-
 829 ides et l'Environnement) and also by the recurrent annual funding provided by the LOPS
 830 parent agencies UBO, CNRS, IRD and Ifremer. This recurrent funding is an important
 831 tool of the French research system that helps fundamental research. The work used HPC
 832 resources from GENCI-TGCC (Grant 2020-A0090112051). The code is available from
 833 <https://doi.org/10.5281/zenodo.4968737>.

834 **References**

- 835 Balsara, D. S., Garain, S., & Shu, C.-W. (2016). An efficient class of weno schemes
 836 with adaptive order. *Journal of Computational Physics*, *326*, 780–804.
- 837 Boris, J., Grinstein, F., Oran, E., & Kolbe, R. (1992). New insights into large eddy
 838 simulation. *Fluid dynamics research*, *10*(4-6), 199.
- 839 Brecht, R., Bauer, W., Bihlo, A., Gay-Balmaz, F., & MacLachlan, S. (2019). Varia-
 840 tional integrator for the rotating shallow-water equations on the sphere. *Quar-
 841 terly Journal of the Royal Meteorological Society*, *145*(720), 1070–1088.
- 842 Chen, Q., Gunzburger, M., & Ringler, T. (2011). A scale-invariant formulation of
 843 the anticipated potential vorticity method. *Monthly Weather Review*, *139*(8),
 844 2614–2629.
- 845 Cotter, C. J., & Thuburn, J. (2014). A finite element exterior calculus framework for
 846 the rotating shallow-water equations. *Journal of Computational Physics*, *257*,
 847 1506–1526.
- 848 Desbrun, M., Kanso, E., & Tong, Y. (2006). Discrete differential forms for computa-
 849 tional modeling. *ACM SIGGRAPH 2006 Courses on - SIGGRAPH '06*. doi:
 850 10.1145/1185657.1185665
- 851 Farge, M., Schneider, K., et al. (2011). Energy dissipating structures produced by
 852 walls in two-dimensional flows at vanishing viscosity. *Physical review letters*,
 853 *106*(18), 184502.
- 854 Frankel, T. (2011). *The geometry of physics: an introduction*. Cambridge university
 855 press.
- 856 Gallerano, F., & Cannata, G. (2011). Central weno scheme for the integral form
 857 of contravariant shallow-water equations. *International Journal for Numerical
 858 Methods in Fluids*, *67*(8), 939–959.
- 859 Gottlieb, S., Shu, C.-W., & Tadmor, E. (2001). Strong stability-preserving high-
 860 order time discretization methods. *SIAM review*, *43*(1), 89–112.
- 861 Graham, J. P., & Ringler, T. (2013). A framework for the evaluation of turbulence
 862 closures used in mesoscale ocean large-eddy simulations. *Ocean Modelling*, *65*,
 863 25–39.
- 864 Jiang, G.-S., & Shu, C.-W. (1996). Efficient implementation of weighted eno
 865 schemes. *Journal of computational physics*, *126*(1), 202–228.
- 866 Keetels, G. H., D’Ortona, U., Kramer, W., Clercx, H. J., Schneider, K., & van Hei-

- 867 jst, G. J. (2007). Fourier spectral and wavelet solvers for the incompressible
 868 navier–stokes equations with volume-penalization: Convergence of a dipole–
 869 wall collision. *Journal of Computational Physics*, *227*(2), 919–945.
- 870 Klöwer, M., Düben, P., & Palmer, T. (2020). Number formats, error mitigation, and
 871 scope for 16-bit arithmetics in weather and climate modeling analyzed with a
 872 shallow water model. *Journal of Advances in Modeling Earth Systems*, *12*(10),
 873 e2020MS002246.
- 874 Lam, S. K., Pitrou, A., & Seibert, S. (2015). Numba: A llvm-based python jit com-
 875 piler. In *Proceedings of the second workshop on the llvm compiler infrastructure*
 876 *in hpc* (pp. 1–6).
- 877 Lattner, C., & Adve, V. (2004). Llvm: A compilation framework for lifelong pro-
 878 gram analysis & transformation. In *International symposium on code genera-*
 879 *tion and optimization, 2004. cgo 2004.* (pp. 75–86).
- 880 Margolin, L. G., Rider, W. J., & Grinstein, F. F. (2006). Modeling turbulent flow
 881 with implicit les. *Journal of Turbulence*(7), N15.
- 882 Mullen, P., McKenzie, A., Pavlov, D., Durant, L., Tong, Y., Kanso, E., . . . Des-
 883 brun, M. (2011). Discrete lie advection of differential forms. *Foundations of*
 884 *Computational Mathematics*, *11*(2), 131–149.
- 885 Noelle, S., Xing, Y., & Shu, C.-W. (2007). High-order well-balanced finite volume
 886 weno schemes for shallow water equation with moving water. *Journal of Com-*
 887 *putational Physics*, *226*(1), 29–58.
- 888 Perot, J. B., & Zusi, C. J. (2014). Differential forms for scientists and engineers.
 889 *Journal of Computational Physics*, *257*, 1373–1393.
- 890 Pope, S. B. (2004). Ten questions concerning the large-eddy simulation of turbulent
 891 flows. *New journal of Physics*, *6*(1), 35.
- 892 Pressel, K. G., Kaul, C. M., Schneider, T., Tan, Z., & Mishra, S. (2015). Large-eddy
 893 simulation in an anelastic framework with closed water and entropy balances.
 894 *Journal of Advances in Modeling Earth Systems*, *7*(3), 1425–1456.
- 895 Ramadhan, A., Wagner, G. L., Hill, C., Campin, J.-M., Churavy, V., Besard, T.,
 896 . . . Marshall, J. (2020). Oceananigans.jl: Fast and friendly geophysical
 897 fluid dynamics on gpus. *Journal of Open Source Software*, *5*(53), 2018. doi:
 898 10.21105/joss.02018
- 899 Ringler, T. D., Thuburn, J., Klemp, J. B., & Skamarock, W. C. (2010). A uni-

- 900 fied approach to energy conservation and potential vorticity dynamics for
 901 arbitrarily-structured c-grids. *Journal of Computational Physics*, 229(9),
 902 3065–3090.
- 903 Roullet, G. (2021, June). *pyRSW: A Fast Monotone Rotating Shallow Water model*.
 904 Zenodo. Retrieved from <https://doi.org/10.5281/zenodo.4968737> (The
 905 code is maintained on <https://github.com/pvthinker/pyRSW>) doi: 10.5281/
 906 zenodo.4968737
- 907 Sadourny, R., & Basdevant, C. (1985). Parameterization of subgrid scale barotropic
 908 and baroclinic eddies in quasi-geostrophic models: Anticipated potential vortic-
 909 ity method. *Journal of Atmospheric Sciences*, 42(13), 1353–1363.
- 910 Sagaut, P. (2006). *Large eddy simulation for incompressible flows: an introduction*.
 911 Springer.
- 912 Shchepetkin, A. F., & McWilliams, J. C. (2005). The regional oceanic modeling
 913 system (roms): a split-explicit, free-surface, topography-following-coordinate
 914 oceanic model. *Ocean modelling*, 9(4), 347–404.
- 915 Shu, C.-W. (1999). High order eno and weno schemes for computational fluid
 916 dynamics. In *High-order methods for computational physics* (pp. 439–582).
 917 Springer.
- 918 Thuburn, J., Ringler, T. D., Skamarock, W. C., & Klemp, J. B. (2009). Numerical
 919 representation of geostrophic modes on arbitrarily structured c-grids. *Journal*
 920 *of Computational Physics*, 228(22), 8321–8335.
- 921 Tsoutsanis, P., Titarev, V. A., & Drikakis, D. (2011). Weno schemes on arbitrary
 922 mixed-element unstructured meshes in three space dimensions. *Journal of*
 923 *Computational Physics*, 230(4), 1585–1601.
- 924 Williams, S., Waterman, A., & Patterson, D. (2009). Roofline: an insightful visual
 925 performance model for multicore architectures. *Communications of the ACM*,
 926 52(4), 65–76.
- 927 Williamson, D. L., Drake, J. B., Hack, J. J., Jakob, R., & Swarztrauber, P. N.
 928 (1992). A standard test set for numerical approximations to the shallow water
 929 equations in spherical geometry. *Journal of Computational Physics*, 102(1),
 930 211–224.
- 931 Xing, Y., & Shu, C.-W. (2005). High order finite difference weno schemes with the
 932 exact conservation property for the shallow water equations. *Journal of Com-*

933 *putational Physics*, 208(1), 206–227.

934 Zhou, Y., Grinstein, F. F., Wachtor, A. J., & Haines, B. M. (2014). Estimating the
935 effective reynolds number in implicit large-eddy simulation. *Physical Review E*,
936 89(1), 013303.